Muon Imaging of Volcanic Conduit Explains Link between Eruption Frequency and Ground Deformation

László Oláh[1,9], Giuseppe Gallo[2,9], Gergő Hamar[3,9], Osamu Kamoshida[4,9], Giovanni Leone[5,9], Edward W. Llewellin[6], Domenico Lo Presti[2,7,9], Gábor Nyitrai[3,8,9], Takao Ohminato[1], Shouhei Ohno[4], Hiroyuki K. M. Tanaka[1,9], Dezső Varga[3,9]

[1]Earthquake Research Institute, The University of Tokyo, Tokyo, Japan
[2]Department of Physics and Astronomy "E. Majorana", University of Catania, Catania, Italy
[3]Institute for Particle and Nuclear Physics, Wigner Research Centre for Physics, Budapest, Hungary
[4]NEC Corporation, Tokyo, Japan
[5]The University of Atacama, Copiapó, Chile
[6]Department of Earth Sciences, Durham University, Durham, UK
[7]National Institute for Nuclear Physics, Catania, Italy
[8]Faculty of Natural Sciences, Budapest University of Technology and Economics, Budapest, Hungary
[9]International Virtual Muography Institute, Global

Key Points:

- An inverse correlation was observed between eruption frequency and ground surface deformation of Sakurajima volcano
- Beneath the crater, muon imaging visualized that the mass density increased during ground inflation and decreased during ground deflation
- Plugging of the conduit with dense, stiff magma during recharge caused inflation during quiescent periods

Corresponding author: László Oláh, `olah.laszlo@wigner.hu`

Abstract

An inverse correlation was observed between eruption frequency and ground surface deformation of Sakurajima volcano (Japan) during November 2018 to April 2021. Over the same period, the mass density of magma in the upper conduit of the active crater was monitored via muography. Mass density increased significantly during inflation, when eruption frequency was low, and decreased during deflation, when eruption frequency was high. On the basis of the muography data, we find that periods of low eruption frequency are associated with the formation of a dense plug in the shallow conduit, which we infer caused inflation of the edifice by trapping pressurized magmatic gas. Conversely, periods of high eruption frequency are associated with the absence of a dense plug, which we infer allows gas to escape, leading to deflation. Muography thus reveals the in-conduit physical mechanism for the observed correlation, with implications for interpretation of deformation at other volcanoes.

Plain Language Summary

Monitoring changes in the ground-surface level at volcanoes can indicate changes in the likelihood of an eruption. In order to be confident of interpretations of monitoring data, we must understand the physical cause of the observed changes and their relation to ongoing volcanic phenomena. We measured changes in mass density in the magmatic plumbing system beneath Sakurajima volcano (Japan) using muons, which are cosmic particles that pass easily through rock. We detected muons that passed through Sakurajima, and constructed images of the density during dormant and active periods, and used this to explain the link between changes in the ground surface level and the number of eruptions. We found that the mass density increased during the dormant periods, when the ground surface of the volcano was high, and the mass density decreased during periods of frequent eruption, when the ground surface was low. Muon imaging helped to reveal the hidden volcanic processes: the volcano plugged during the dormant periods and recharge of fresh magma into the conduit resulted in uplift of the volcano's surface. During periods of eruption, gas pockets formed within the plug, driving explosions, and the release of pressure resulted in the downlift of the volcano's surface.

1 Introduction

Forecasting the location, onset, cessation and style of impending volcanic eruptions facilitates effective mitigation of the impact of associated hazards (Sparks, 2003; Poland & Anderson, 2020). Active volcanism is driven by the subsurface evolution and movement of magmatic materials, which may induce seismicity (Chouet, 1996; Brenguier et al., 2008; Dempsey et al., 2020), ground deformation (Biggs et al., 2014, 2016), gas emission (Fischer et al., 1994; Werner et al., 2013), and fumarolic activity (Francis et al., 1980). Monitoring of the signals induced by these phenomena is indirect and interpretation of the origin of the signals is challenging because a wide variety of factors influence the behaviour of magma and host rock in the run-up towards eruption (Woods & Koyaguchi, 1994; Melnik & Sparks, 2002; Caricchi et al., 2014). The complex structure of volcanic systems and the stochastic nature of the driving processes mean that interpretation of monitoring signals typically relies on correlation, rather than causation. This hinders the detection and interpretation of pre-eruptive phenomena (Sano et al., 2015) and may results in 'false positives': activity that is interpreted as a precursor, which does not foreshadow an eruption (Syahbana et al., 2019). The observed correlations between monitoring signals and eruptive activity would be more robust if they could be linked via the casual physical mechanism.

Near-real-time observations of ground surface deformations have revealed both subsidence of volcanic edifices during eruption (Massonnet et al., 1995) and inflation of volcanic edifices during quiescent periods preceding an eruption (Patané et al., 2003). Such data sets have provided insights into how edifice deformation is linked to volcanism (Biggs et al., 2014; Pinel et al., 2014). For instance, Biggs et al. (2014) present a probabilistic analysis of interferometric synthetic aperture radar (InSAR) data collected at 198 volcanoes over an 18 year period, which showed that 94 % of the volcanoes that did not deform also did not erupt, whereas 46 % of volcanoes that deformed also erupted (tectonic changes induced the remaining deformations). Modelling of magma flow and viscosity changes and pressure changes occurring in the upper part of conduit have been used to link short-term eruptive cycles to observed ground deformations, but the outcomes are not always predictable (Albino et al., 2011). Combining ground deformation measurements with other sensitive techniques can help us to understand the causal physical mechanism by which ground deformation and volcanic activity are linked, and lead towards more robust and predictive interpretations of the monitoring signals. Geophysical monitoring of combined magma and host rock mass density can reveal the underlying physical mechanism of volcanic activity by providing indirect information about the composition and spatio-temporal evolution of magma propagation to the surface (Poland & Carbone, 2016; Londoño & Kumagai, 2018). Here we use of muon imaging to determine changes in density in the plumbing system of Sakurajima volcano (Kyushu, Japan) at high spatial and temporal resolution, and relate the results to observations of both ground deformation and eruptive activity.

Eruptions at Sakurajima are dominantly vulcanian, comprising impulsive explosions that typically last minutes-to-hours (Iguchi et al., 2008; Miwa & Toramaru, 2013; Yokoo et al., 2013). Activity is cyclic, with typical inter-eruption interval of a few days (Gabellini et al., 2022). Since 2006, eruptive activity at Sakurajima has alternated between the Minamidake crater and the Showa crater (Japan Meteorological Agency, 2022). Periods of relatively high eruption frequency at a particular crater alternate with periods of quiescence – both periods typically last for several months. The physical mechanism for the hours-to-days cycles of vulcanian explosions has been extensively investigated through analysis of visual observations, seismic and geodetic data, gas geochemistry data, and characterization of eruption products (Iguchi et al., 2008; Miwa & Toramaru, 2013; Yokoo et al., 2013; Gabellini et al., 2022). The prevailing physical model infers the presence of a dense plug of viscous magma in the upper few tens of meters of the conduit, beneath which a pressurized pocket of gas accumulates, which is a few hundred meters in vertical extent; explosions result from failure of the plug (Iguchi et al., 2008; Miwa & Toramaru, 2013; Yokoo et al., 2013; Kazahaya et al., 2016; Gabellini et al., 2022). Similar mechanisms have been invoked to explain vulcanian activity at other volcanoes, including Semeru (Java, Indonesia), Suwanosejima (Kyushu, Japan), and Soufrière Hills (Montserrat, West Indies) among others (Watt et al., 2007; Iguchi et al., 2008; Burgisser et al., 2011). The longer-term cycles of alternating periods of high and low eruption frequency have received much less attention. Gabellini et al. (2022) study the morphological and petrological characteristics of ash emitted during vulcanian activity at Sakurajima, and conclude that the dense, viscous plug forms over a period of several months, characterized by quiescence or low eruptive frequency, and is progressively destroyed during periods of high eruption frequency. In this work, we use muography to investigate these longer cycles.

2 Muon imaging of volcanic interior

Muography exploits naturally occurring cosmic-ray muons to reconstruct the average densities along the paths of muons across large-scale structures, producing muon "radiographic" images (Tanaka et al., 2007). The constant flux and the high penetration power of muons allow passive and remote imaging of the shallow density structures in volcanoes at a spatial resolution of few meters (Nishiyama et al., 2014; Oláh et al., 2018; Macedonio et al., 2022; Miyamoto et al., 2022). Muography has already been used to image the spatio-temporal evolution of magmatic materials, – e.g., ascent and descent of magma within a volcanic vent (Tanaka et al., 2014), magma degassing (Tanaka et al., 2009) and plug formation underneath deactivated craters (Oláh et al., 2019) – and to observe structural changes (Lo Presti et al., 2022; Tioukov et al., 2022) and hydrothermal activities (Gibert et al., 2022) in volcanic systems. The early warning capabilities of muography have also been studied (Nomura et al., 2020; Leone et al., 2021; Oláh & Tanaka, 2022a). We conducted muography of Sakurajima volcano over the period from September 2018 to July 2021.

The elevation map of the observational site and schematic drawing of the experimental configuration are shown in Figure 1. We applied the Multi-Wire Proportional Chamber-based Muography Observation System (MMOS) (Oláh et al., 2018; Varga et al., 2020, 2022) of Sakurajima Muography Observatory for muographic monitoring of mass density changes underneath the active craters (Text S1 in the supporting information). The small black rectangle shows the location of the observatory (O) at latitude 31.557 °N and longitude 130.650 °E, at altitude 150 m above sea level. The MMOS was oriented towards the active craters at 30.25° from north (defined as $\tan(\theta_X) = 0$), as shown by the black arrow, and set to horizontal (defined as $\tan(\theta_Y) = 0$). The MMOS collected muon tracks within ±505 mrad in the horizontal direction and ±353 mrad in the vertical direction. The points M, S, and R were selected on the northeast slope of the volcano to extract three cross-sections across Minamidake crater, Showa crater and Reference region, respectively. Figure 1b shows the three selected cross-sections along the OM, OS and OR lines. The targeted region underneath the active crater is shown within the OP and OQ lines. We note that the vertical angle region of 0-150 mrad (see under the OP line) was also covered by the MMOS, but the excessive (> 2.5 km) rock thickness did not allow us to measure the density in this angular region beneath the crater. The MMOS measured the muon tracks continuously from January 2017 with only a few technical stops of a few days each during installation of new MMOS modules or maintenance work (Oláh et al., 2019, 2021; Varga et al., 2020).

The data from the MMOS were processed to create muographic images that show the density structure through the crater region of Sakurajima volcano. Muographic images use the natural coordinate system of the MMOS that is the tangents of the projections of incoming muon directions with respect to the orientation of MMOS: $\tan(\theta_X)$ and $\tan(\theta_Y)$ (Text S1 in the supporting information). Each muographic image was captured with a binning of 0.023 (that corresponds to a spatial resolution of approx. 60 m at the crater, which is located at a distance of 2.65 km from the MMOS) in both horizontal and vertical directions. Each image was determined for a period of five months. The muographic image processing was based on comparison of modelled and measured muon fluxes. The measured trajectories of particles were reconstructed by 1+1-dimensional line fits onto coordinates on the tracking layers (Oláh et al., 2018), and the fluxes were calculated for each angular bins by taking into account the measurement time, dead time, and detector geometry (Oláh et al., 2019). Quality assurance of the data was performed by offline analysis and low-quality data were removed from the analyzed data sets. The modelled fluxes were determined by integrating the differential muon spectra (Tang et al., 2006) from the threshold energies that were required for muons to penetrate through the volcanic edifice. The threshold energies were calculated (Oláh et al., 2021) by taking into account the stochastic energy loss processes of muons (Lipari & Stanev, 1991).

3 Results

Figures 2a-x show images selected from a period between November 2018 and March 2021. The blue dashed line visualizes the shape of the crater along the blue dashed line of Figure 1a. Black rectangular outlines highlight a region underneath the active Minamidake crater (M), a region underneath the dormant Showa crater (S) and a Reference region (R) in which volcanism does not occur. The vertical range of these regions corresponds to the angular region between the OP and OQ lines in Figure 1a. The path-averaged densities (ρ) ranged between 0.8 gcm^{-3} and 1.8 gcm^{-3} through the regions underlying Minamidake crater and Showa crater. Density values ranged from 0.8 gcm^{-3} to 1.25 gcm^{-3} through the Reference region. The lower densities through the Reference region likely arises because energetic (>1 GeV) muons scattered into the MMOS from the surface of the downward sloping parts of volcanic edifice (Ambrosino et al., 2015). The white-shaded regions without density values are due to the thickness that was not penetrated by muons during the data collection time. The muographic images show that the densities change over time through the region underneath the craters.

Vertical displacement of the volcanic edifice was determined over the same period as the muography measurements (e.g., red line in Figure 2y). Displacement was determined relative to the ground level measured on 31 October 2018 at ten locations (red-coloured dots in Figure 1b) using the Phased Array type C-band Synthetic Aperture Radar images acquired by Sentinel-1 (The European Space Agency, 2022). Eruption frequency for each crater, over the same time period, was determined from the data base of Japan Meteorological Agency (2022). We found that ground level, averaged monthly, at the Minamidake crater (location 8 in Figure 1b and red-coloured line in Figure 2y) and eruption frequencies, binned monthly, correlated inversely with a Pearson's coefficient of -0.718 (Spearman's rank coefficient of -0.798). We found moderate and weak inverse correlations for the same quantities at the locations 1, 2, 3 and 9 with coefficients of -0.547 (-0.595), -0.509 (-0.432), -0.514 (-0.421) and -0.564 (-0.685), respectively. No significant correlation was found at the remaining locations. Visual inspection of Figure 2 suggests that density beneath the active craters is high during periods of low eruption frequency and upward displacement of the ground surface, and vice versa.

The muographically measured density values were averaged for the three regions (M, S, R in Figure 2) to quantify their variations in relation to the eruption frequencies and ground deformation during periods of high eruption frequency and periods of quiescence. Figures 3a-c show together: 1) five month average of densities with one standard deviation relative to the densities measured for the first time sequence from 1 September 2018 to 31 January 2019 ($\Delta\rho$=ρ(t)-ρ(t0), where ρ(t0) equals to 1.26 gcm^{-3}, 1.13 gcm^{-3} and 0.99 gcm^{-3} for the Minamidake crater, Showa crater and Reference region, respectively); 2) the monthly number of eruptions (black histogram); and 3) the vertical ground displacement (red-coloured lines) for each region. The relative density increased beneath the Minamidake crater (Figure 3a) throughout the periods of inflation and reduced eruption frequency (from March to September 2019 and from August 2020 to January 2021). The increase of average relative densities exceeded 0.2-0.35 gcm^{-3} which is significantly above the systematic density error of 0.06 gcm^{-3} (see in Oláh and Tanaka (2022b) and Text S1 in the supporting information). The relative densities decreased beneath the Minamidake crater during periods in which the volcanic edifice deflated and the eruption frequency increased (from November 2019 to May 2020 and from November 2020 to May 2021).

The densities beneath the dormant Showa crater (Figure 3b) slightly increased at the end of 2018 and remained below 0.1 gcm^{-3} during the observations periods. Across the Reference region (Figure 3c), the density changes were below 0.1 gcm^{-3}.

4 Discussion

We monitored the mass density changes through the upper conduit of Sakurajima volcano with muography during cyclic eruption episodes of Minamidake crater. We found that the trends in mass density were linked to trends in ground deformation and eruption frequency: the mass density increased during periods of inflation and low eruption frequency, and decreased during periods of deflation and high eruption frequency. These observed trends also correlate with other monitoring signals. During the periods from January to July 2019 and from June to November 2020 (roughly coincident with periods of high density, edifice inflation, and low eruption frequency), the time series of the vertical locations of seismic sources distributed at shallow depths underneath the Minamidake crater (middle right panel of Figure 3 in Japan Meteorological Agency (2021)) that also suggested the densification of this region. Furthermore, infrared thermal imaging revealed high-temperature regions in the Minamidake crater in August 2020 (Figure 3-1 in Japan Meteorological Agency (2020)), and glowing of Minamidake was observed in September and October 2020 (Figures 4-1, 4-2 in Japan Meteorological Agency (2020)). During periods of low density, edifice deflation, and high eruption frequency, increased trends were observed in the sulphur dioxide discharge mass rate by JMA (upper panel of Figure 8-2 in Japan Meteorological Agency (2021)).

The increase in mass density revealed by the muography data is consistent with the formation of a dense plug of magma in the shallow plumbing system (upper ~ 200 m) of Minamidake crater during periods of low eruption frequency, as proposed by Gabellini et al. (2022). Upward deformation of the volcanic edifice during this period is consistent with slow upward migration of the dense, stiff plug driven by pressure from below as the conduit refills with fresh magma. We note that five highly energetic explosions occurred in June 2020 (i.e., at the start of a period of inflation) from which volcanic ejecta reached the altitude of 1.5-3.7 km above the crater rim (Japan Meteorological Agency, 2020). These events may have been associated with the onset of magma intrusion into the gas pocket. The observations of high-temperature regions and glowing material in the crater indicates that portions of the dense, hot plug are extruded into the crater. Conversely, the decrease in mass density during periods of high eruption frequency is consistent with the presence of gas pockets in the conduit, as proposed in numerous studies (e.g., Iguchi et al. (2008), Miwa and Toramaru (2013), Yokoo et al. (2013), Kazahaya et al. (2016)). The associated deflation of the edifice may result from the cessation of recharge of magma, and the progressive outgassing of the magma within the conduit. This is consistent with the elevated sulphur dioxide discharge mass rate measured during these periods (Japan Meteorological Agency, 2020).

Concerning the Showa crater, the observed slight density increase is assumed to be a part of the plug formation process (Oláh et al., 2019) initiated at the end of 2017 by cessation of eruptive activity (Japan Meteorological Agency, 2022). Although the vertical uplifts increased from 2018 December to June 2020, no significant change was in the trend of density was observed during this period. The minor density changes ($< 0.1\,\mathrm{gcm}^{-3}$) in the Reference region are consistent with its non-magmatic nature, and act as a control.

Lo Presti et al. (2022) measured the muon flux through the Northeast crater and the Voragine crater of Mount Etna at latitude 37.757 °N and longitude 14.988 °E. Data acquisition was conducted from July to November in 2018 (95 days) and between August and September in 2019 (51 days). The forward (volcano's direction) to backward (opposite to volcano's direction) muon flux ratios (C) were quantified for both periods. Figure 4 shows the ratio of the C measured in 2019 (C_{2019}) to the C measured in 2018 (C_{2018}) in the natural coordinate system of the muon tracker (same as the coordinate system of Figures 2a-x). The cross-sectional presentation of the crater floor in Etna is not shown in this figure since it was difficult for us to acquire the elevation data presenting the topographic shape right before the 2019 volcanic activity. This muographic image shows a region through the Voragine crater in which the C increased from 2018 to 2019. The increase in C represents the decrease in mass density. The eruption frequency of the Voragine crater increased also (Global Volcanism Program, 2022; National Institute of Geophysics and Volcanology, 2022): the crater did not erupt since December 2015. A new vent opened in August 2018 and degassing from the new vent initiated in January 2019. Another new vent opened in April 2019 from which two eruption sequences occurred in June and September 2019. Near surface relative density reduction observed at Voragine crater during the 2019 eruptions is in agreement with the relative density reduction we observed during the eruptions of Sakurajima. A joint muographic observation of the two volcanoes will may provide more insights into the shallow volcanic processes.

5 Conclusions and outlook

In this work we have demonstrated that muography can be a valuable tool for investigating in-conduit processes at active volcanoes, particularly when combined with other monitoring data. The technique provides data for the evolution of mass density of magma in the shallow conduit at sufficiently high temporal and spatial resolution that changes in the eruption can be associated with changes in the state of the magma in the shallow conduit. This has great potential for elucidating the mechanisms through which changes in eruption frequency are mediated by physical processes in the shallow conduit which, in turn, will improve conceptual, physical, and numerical models of eruptive processes. Vulcanian activity similar to that at Sakurajima is common at volcanoes worldwide, and similar conceptual models for eruption activity have been proposed (e.g., Watt et al. (2007), Iguchi et al. (2008), Burgisser et al. (2011)). The model for long-period (multi-month) changes in eruptive activity that we develop here could therefore be applicable elsewhere.

This work also indicates that muography could be used to improve the intermediate-term assessment of the hazard levels at stratovolcanoes by allowing more meaningful interpretation of InSAR data. For instance, where edifice inflation is associated with an increase in magma density in the shallow conduit, it could indicate a plugging of the shallow conduit and the onset of a period of reduced eruption frequency. Furthermore, muography has the potential for providing useful data even between the observation flights of space-borne InSAR for detecting rapid (a few days duration) changes in magma conditions underneath the active craters. Currently, the main limitation in muography is the relatively long measurement time; this can be reduced by enlarging the sensitive surface area of the available muographic observation systems, and we anticipate that technological improvements in muography will further enhance its value to volcanology.

Acknowledgments

This work was supported by the Joint Usage Research Project (JURP) of the University of Tokyo, Earthquake Research Institute (ERI) under project ID 2020-H-05, the Hungarian NKFIH research grants under identification numbers OTKA-FK-135349 and TKP2021-NKTA-10, the ELKH KT SA-88/2021 research grant; and the Ministry of Education, Culture, Sports, Science and Technology, Japan (MEXT) Integrated Program for the Next Generation Volcano Research; and and the "INTENSE" H2020 MSCA RISE, GA No. 822185. G.H. is supported by the János Bolyai Research Scholarship of the HAS. The technical support provided by the members of the REGARD group is gratefully acknowledged. **Author Contributions:** L.O. and H.K.M.T. conceived the study. L.O., G.H., G.Ny., H.K.M.T. and D.V. conducted the muographic observation of Sakurajima volcano. L.O. analysed of muographic data of Sakurajima volcano. S.O. and K.O. analysed the InSAR data. E.W.L., L.O. and H.K.M.T. interpreted the observations. L.O. drafted the figures. G.G. and D.L.P. produced the data of figure 4. L.O. lead the writing of the manuscript with contributions from all authors. **Data Availability Statement:** The datasets of this study are available in a repository at following link: `https://osf.io/tws4j/?view_only=43ce27d1d94647eeaea9c3cdd117fe70`.

References

Albino, F., Pinel, V., Massol, H., & Collombet, M. (2011). Conditions for detection of ground deformation induced by conduit flow and evolution. *J. Geophys. Res.*

Solid Earth, *116*, B06201.
Ambrosino, F., Anastasio, A., Bross, A., Béné, S., Boivin, P., Bonechi, L., ... Vulpescu, B. (2015). Joint measurement of the atmospheric muon flux through the Puy de Dôme volcano with plastic scintillators and Resistive Plate Chambers detectors. *J. Geophys. Res. Solid Earth*, *120*, 7290-7307.
Biggs, J., Ebmeier, S. K., Aspinall, W. P., Lu, Z., Pritchard, M. E., Sparks, R. S. J., & Mather, T. A. (2014). Global link between deformation and volcanic eruption quantified by satellite imagery. *Nat. Commun.*, *5*, 3471.
Biggs, J., Robertson, E., & Cashman, C. (2016). The lateral extent of volcanic interactions during unrest and eruption. *Nat. Geosci.*, *9*, 308-311.
Brenguier, F., Shapiro, N. M., Campillo, M., Ferrazzini, V., Duputel, Z., Coutant, O., & Nercessian, A. (2008). Towards forecasting volcanic eruptions using seismic noise. *Nat. Geosci.*, *1*, 126-130.
Burgisser, A., Arbaret, L., Druitt, T. H., & Giachetti, T. (2011). Pre-explosive conduit conditions of the 1997 Vulcanian explosions at Soufrière Hills Volcano, Montserrat: II. Overpressure and depth distributions. *J. Volcanol. Geotherm. Res.*, *199*, 193-205.
Caricchi, L., Blundy, J., Simpson, G., & Pinel, V. (2014). Frequency and magnitude of volcanic eruptions controlled by magma injection and buoyancy. *Nat. Geosci.*, *7*, 126-130.
Chouet, B. (1996). Long-period volcano seismicity: its source and use in eruption forecasting. *Nature*, *380*, 309-316.
Dempsey, D. E., Cronin, S. J., Mei, S., & Kempa-Liehr, A. W. (2020). Automatic precursor recognition and real-time forecasting of sudden explosive volcanic eruptions at Whakaari, New Zealand. *Nat. Commun.*, *11*, 3562.
Fischer, T. P., Morrissey, M. M., Marta Lucía Calvache, V., Diego Gómez, M., Roberto Torres, C., Stix, J., & Williams, S. N. (1994). Correlations between SO_2 flux and long-period seismicity at Galeras volcano. *Nature*, *368*, 135-137.
Francis, P., Thorpe, R., & Brown, G. (1980). Pyroclastic sulphur eruption at Poas volcano, Costa Rica. *Nature*, *283*, 754-756.
Gabellini, P., Cioni, R., Geshi, N., Pistolesi, M., Miwa, T., Lacanna, G., & Ripepe, M. (2022). Eruptive dynamics and fragmentation mechanisms during cyclic Vulcanian activity at Sakurajima volcano (Japan): Insights from ash texture analysis. *J. Volcanol. Geotherm. Res.*, *428*, 107582.
Gibert, D., de Bremond d'Ars, J., Carlus, B., Deroussi, S., Ianigro, J.-C., Jessop, D. E., ... Rosas-Carbajal, M. (2022). Observation of the Dynamics of Hydrothermal Activity in La Soufrière of Guadeloupe Volcano with Joint Muography, Gravimetry, Electrical Resistivity Tomography, Seismic and Temperature Monitoring. *Geophys. Mon. Ser.*, *270*, 55-73.
Global Volcanism Program. (2022). *Bulletin Report about Mount Etna.* Retrieved from `https://volcano.si.edu/volcano.cfm?vn=211060&vtab=Bulletin` ([Online; accessed 7-September-2022])
Iguchi, M., Yakiwara, H., Tameguri, T., Hendrasto, M., & Hirabayashi, J. (2008). Mechanism of explosive eruption revealed by geophysical observations at the Sakurajima, Suwanosejima and Semeru volcanoes. *J. Volcanol. Geotherm. Res.*, *178*, 1-9.
Japan Meteorological Agency. (2020). Report of 147th Coordinating Committee of Prediction of Volcanic Eruption. Retrieved from `https://www.data.jma.go.jp/svd/vois/data/tokyo/STOCK/kaisetsu/CCPVE/shiryo/147/147_2-1.pdf` ([Online; accessed 26-August-2022])
Japan Meteorological Agency. (2021). Report of 149th Coordinating Committee of Prediction of Volcanic Eruption. Retrieved from `https://www.data.jma.go.jp/svd/vois/data/tokyo/STOCK/kaisetsu/CCPVE/shiryo/149/149_2-1.pdf` ([Online; accessed 26-August-2022])
Japan Meteorological Agency. (2022). *Monthly data of Sakurajima eruptions.*

Retrieved from `https://www.jma-net.go.jp/kagoshima/vol/data/skr_erp_num.html`
Kazahaya, R., Shinohara, H., Mori, T., Iguchi, M., & Yokoo, A. (2016). Pre-eruptive inflation caused by gas accumulation: Insight from detailed gas flux variation at Sakurajima volcano, Japan. *Geophys. Res. Lett.*, *43*, 11219-11225.
Leone, G., Tanaka, H. K. M., Holma, M., Kuusiniemi, P., Varga, D., Oláh, L., ... Joutsenvaara, J. (2021). Muography as a new complementary tool in monitoring volcanic hazard: implications for early warning systems. *Proc. R. Soc. A*, *477*, 20210320.
Lipari, P., & Stanev, T. (1991). Propagation of multi-TeV muons. *Phys. Rev. D*, *44*, 3543.
Londoño, J. M., & Kumagai, H. (2018). 4D seismic tomography of Nevado del Ruiz Volcano, Colombia, 2000-2016. *J. Volcanol. Geotherm. Res.*, *358*, 105-123.
Lo Presti, D., Gallo, G., Bonanno, D. L., Bonanno, G., Ferlito, C., La Rocca, P., ... Romeo, G. (2022). Three Years of Muography at Mount Etna, Italy: Results and Interpretation. *Geophys. Mon. Ser.*, *270*, 93-108.
Macedonio, G., Saracino, G., Ambrosino, F., Baccani, G., Bonechi, L., Bross, A., ... Viliani, L. (2022). Muography of the Volcanic Structure of the Summit of Vesuvius. *Geophys. Mon. Ser.*, *270*, 123-136.
Massonnet, D., Briole, P., & Arnaud, A. (1995). Deflation of Mount Etna monitored by spaceborne radar interferometry. *Nature*, *375*, 567-570.
Melnik, O., & Sparks, R. S. J. (2002). Dynamics of magma ascent and lava extrusion at Soufrière Hills Volcano, Montserrat. *Geo. Soc., London, Memoirs*, *21*, 153-171.
Miwa, T., & Toramaru, A. (2013). Conduit process in vulcanian eruptions at Sakurajima volcano, Japan: Inference from comparison of volcanic ash with pressure wave and seismic data. *Bulletin of Volcanology*, *75(1)*, 1-13.
Miyamoto, S., Nagahara, S., Morishima, K., Nakano, T., Koyama, M., & Suzuki, Y. (2022). A muographic study of a scoria cone from 11 directions using nuclear emulsion cloud chambers. *Geosci. Instrum. Method. Data Syst.*, *11*, 127-147.
National Institute of Geophysics and Volcanology. (2022). *Etna Observatory, Communication of Volcanic Activity.* Retrieved from `https://www.ct.ingv.it/index.php/monitoraggio-e-sorveglianza/prodotti-del-monitoraggio/comunicati-attivita-vulcanica` ([Online; accessed 26-August-2022])
Nishiyama, R., Tanaka, Y., Okubo, S., Oshima, H., Tanaka, H. K. M., & Maekawa, T. (2014). Integrated processing of muon radiography and gravity anomaly data toward the realization of highresolution 3D density structural analysis of volcanoes: Case study of Showa-Shinzan lava dome, Usu, Japan. *J. Geophys. Res. Solid Earth*, *119*, 699-710.
Nomura, Y., Nemoto, M., Hayashi, N., Hanaoka, S., Murata, M., Yoshikawa, T., ... Tanaka, H. K. M. (2020). Pilot study of eruption forecasting with muography using convolutional neural network. *Sci. Rep.*, *10*, 5272.
Oláh, L., & Tanaka, H. K. M. (2022a). Machine Learning with Muographic Images as Input: An Application to Volcano Eruption Forecasting. *Geophys. Mon. Ser.*, *270*, 43-54.
Oláh, L., & Tanaka, H. K. M. (2022b). Muography of magma intrusion beneath the active craters of Sakurajima volcano. *Geophys. Mon. Ser.*, *270*, 109-122.
Oláh, L., Tanaka, H. K. M., & Hamar, G. (2021). Muographic monitoring of hydrogeomorphic changes induced by post-eruptive lahars and erosion of Sakurajima volcano. *Sci. Rep.*, *11*, 17729.
Oláh, L., Tanaka, H. K. M., Ohminato, T., Hamar, G., & Varga, D. (2019). Plug Formation Imaged Beneath the Active Craters of Sakurajima Volcano With Muography. *Geophys. Res. Lett.*, *46*, 10417-10424.
Oláh, L., Tanaka, H. K. M., Ohminato, T., & Varga, D. (2018). High-definition and low-noise muography of the Sakurajima volcano with gaseous tracking

detectors. *Sci. Rep.*, *8*, 3207.

Patané, D., De Gori, P., Chiarabba, C., & Bonaccorso, A. (2003). Magma Ascent and the Pressurization of Mount Etnas Volcanic System. *Science*, *299*, 2061-2063.

Pinel, V., Poland, M. P., & Hooper, A. (2014). Volcanology: Lessons learned from Synthetic Aperture Radar imagery. *J. Volcanol. Geotherm. Res.*, *289*, 81-113.

Poland, M. P., & Anderson, K. R. (2020). Partly Cloudy With a Chance of Lava Flows: Forecasting Volcanic Eruptions in the Twenty-First Century. *J. Geophys. Res. Solid Earth*, *125*(1), e2018JB016974.

Poland, M. P., & Carbone, D. (2016). Insights into shallow magmatic processes at Kīlauea volcano, Hawai'i, from a multiyear continuous gravity time series. *J. Geophys. Res. Solid Earth*, *121*, 5477-5492.

Sano, Y., Kagoshima, T., Takahata, N., Nishio, Y., Roulleau, E., Pinti, D. L., & Fischer, T. P. (2015). Ten-year helium anomaly prior to the 2014 Mt Ontake eruption. *Sci. Rep.*, *5*, 13069.

Sparks, R. S. J. (2003). Forecasting volcanic eruptions. *Earth Planet. Sci. Lett.*, *210*, 1-15.

Syahbana, D. K., Kasbani, K., Suantika, G., Prambada, O., Andreas, A. S., Saing, U. B., ... Lowenstern, J. B. (2019). The 2017-19 activity at Mount Agung in Bali (Indonesia): Intense unrest, monitoring, crisis response, evacuation, and eruption. *Sci. Rep.*, *9*, 8848.

Tanaka, H. K. M., Kusagaya, T., & Shinohara, H. (2014). Radiographic visualization of magma dynamics in an erupting volcano. *Nat. Comm.*, *5*, 3381.

Tanaka, H. K. M., Nakano, T., Takahashi, S., Yoshida, J., Takeo, M., Oikawa, J., ... Niwa, K. (2007). High resolution imaging in the inhomogeneous crust with cosmic-ray muon radiography: The density structure below the volcanic crater floor of Mt. Asama, Japan. *Earth Planet. Sci. Lett.*, *263*, 104-113.

Tanaka, H. K. M., Uchida, T., Tanaka, M., Shinohara, H., & Taira, H. (2009). Cosmic-ray muon imaging of magma in conduit: Degassing process of Satsuma-Iwojima Volcano, Japan. *Geophys. Res. Lett.*, *36*, L01304.

Tang, A., Horton-Smith, G., Kudryavtsev, V. A., & Tonazzo, A. (2006). Muon simulations for Super-Kamiokande, KamLAND, and CHOOZ. *Phys. Rev. D*, *74*, 053007.

The European Space Agency. (2022). *SAR Instrument.* Retrieved from `https://sentinels.copernicus.eu/web/sentinel/technical-guides/sentinel-1-sar/sar-instrument` ([Online; accessed 26-August-2022])

Tioukov, V., Giudicepietro, F., Macedoni, G., Calvari, S., Di Traglia, F., Fornaciai, A., & Favalli, M. (2022). Structure of the Shallow Supply System at Stromboli Volcano, Italy, through Integration of Muography, Digital Elevation Models, Seismicity, and Ground Deformation Data. *Geophys. Mon. Ser.*, *270*, 75-91.

Varga, D., Hamar, G., Balogh, S., Gera, A., Nyitrai, G., & Surányi, G. (2022). Construction and Readout Systems for Gaseous Muography Detectors. *J. Adv. Inst. Sci.*, *2022*, JAIS-307.

Varga, D., Nyitrai, G., Hamar, G., Galgóczi, G., Oláh, L., Tanaka, H. K. M., & Ohminato, T. (2020). Detector developments for high performance Muography applications. *Nucl. Instrum. Methods Phys. Res. A*, *958*, 162236.

Watt, S. F. L., Mather, T. A., & Pyle, D. M. (2007). Vulcanian explosion cycles: Patterns and predictability. *Geology*, *35(9)*, 839-842.

Werner, C., Kelly, P. J., Doukas, M., Lopez, T., Pfeffer, M., McGimsey, R., & Neal, C. (2013). Degassing of CO_2, SO_2, and H_2S associated with the 2009 eruption of Redoubt Volcano, Alaska. *J. Volcanol. Geotherm. Res.*, *259*, 270-284.

Woods, A. W., & Koyaguchi, T. (1994). Transitions between explosive and effusive eruptions of silicic magmas. *Nature*, *370*, 641-644.

Yokoo, A., Iguchi, M., Tameguri, T., & Yamamoto, K. (2013). Processes Prior to Outbursts of Vulcanian Eruption at Showa Crater of Sakurajima Volcano.

Bull. Volcanol. Soc. Japan, *58*, 163-181.

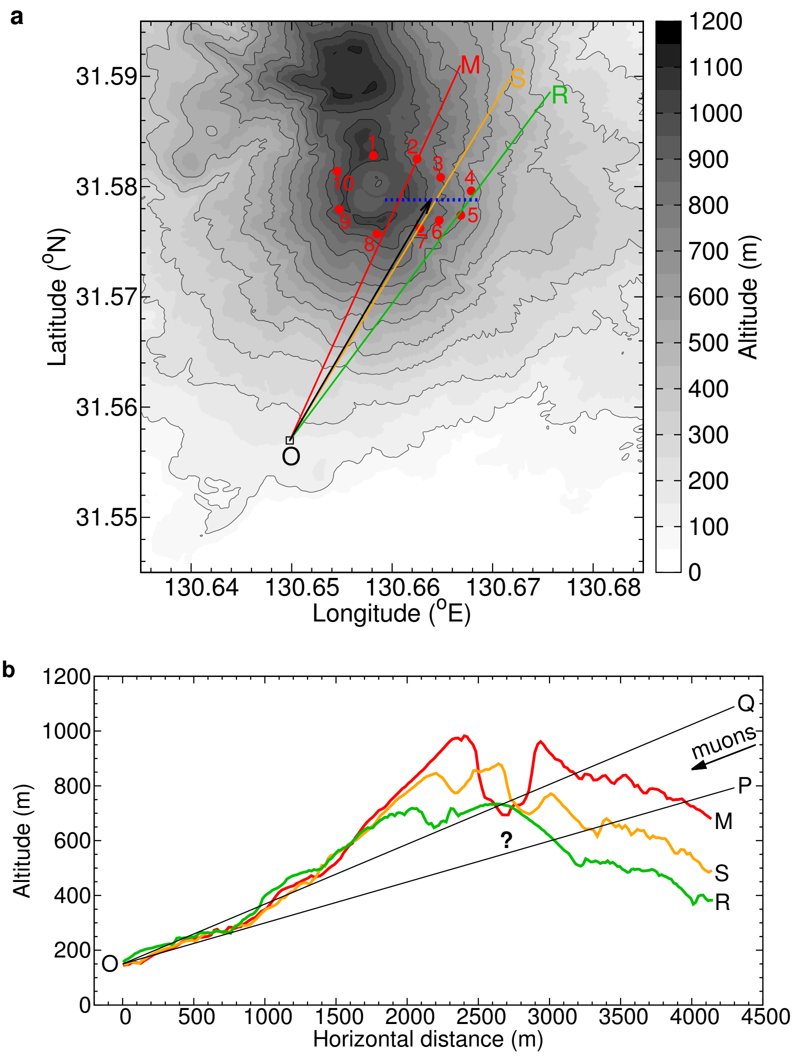

Figure 1. Map of measurement site and schematic of the experimental arrangement. **a,** The map of Sakurajima volcano is drawn based on the digital elevation data of Geospatial Information Authority of Japan (`http://www.gsi.go.jp/`). A small black rectangle shows the location of the muography observatory (O) at latitude 31.557 °N and longitude 130.650 °E, at 150 m altitude above sea level. The black arrow shows the azimuthal orientation of MMOS that was set to 30.25° from north (defined as $\tan(\theta_X) = 0$). The MMOS was oriented horizontally (defined as $\tan(\theta_Y) = 0$). OM, OS, OR lines highlights three selected cross-sections across the Minamidake crater, Showa crater and a Reference region, respectively. The blue dashed line shows a selected cross-section across the crater region. Red-coloured dots and numbers refer respectively to the locations and identification numbers of selected sites where ground displacements were determined from the data collected by synthetic aperture radar. **b,** Three cross-sections of the measurement site are shown along the OM, OS and OR lines, respectively. The OP and OQ lines bound the vertical range of the studied region beneath the craters. Question mark shows the location of volcanic conduits within the studied angular region.

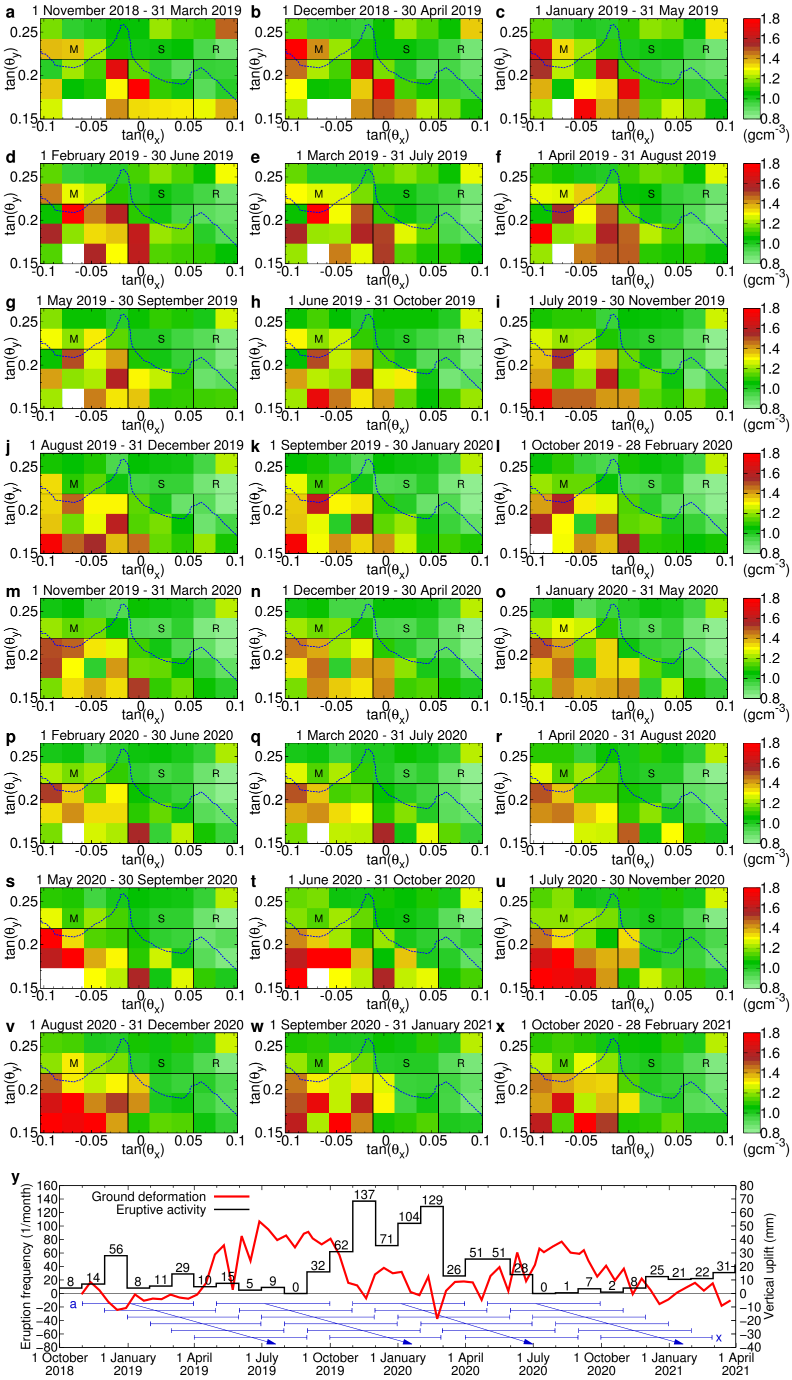

Figure 2. Time-sequential density images of Sakurajima volcano. **a-x,** The average density (ρ) values are plotted for the crater region as a function of horizontal and elevation directions for periods of 5 months from 1 November 2018 to 28 February 2021. The densities were calculated for angular bins with the size of $\Delta(\tan(\theta_X)) \times \Delta(\tan(\theta_Y)) = 0.023 \times 0.023$ each. Blue-coloured dashed lines show the cross-section of craters along the blue-coloured dashed line of Figure 1a. Black rectangular outlines designate three angular regions beneath the Minamidake crater (M), the Showa crater (S) and the Reference region (R), respectively. **y,** Time-lines of ground deformation (red-coloured line) and eruptive frequency (black histogram) are shown for the Minamidake crater of Sakurajima volcano, Japan. Ground deformation data were recorded with InSAR (The European Space Agency, 2022). The eruptive frequency was determined using the data from (Japan Meteorological Agency, 2022). Blue arrows are drawn for comparing the **a-x** images with these time-lines.

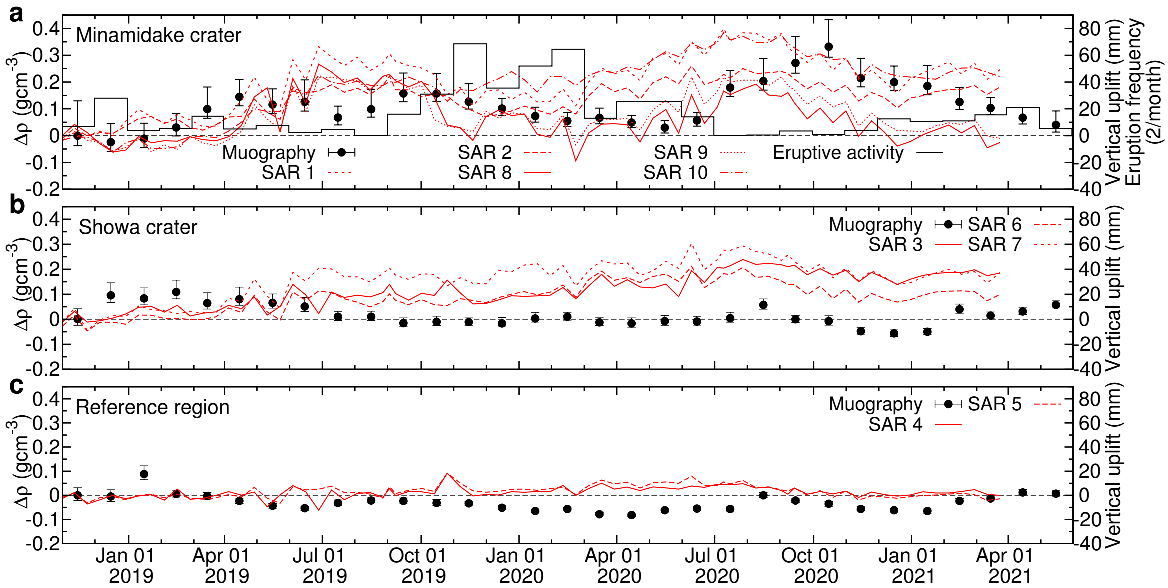

Figure 3. Time evolution of relative averaged densities and vertical uplifts through the three regions of Sakurajima volcano. The densities are shown with 1 standard deviation error bars from September 2018 to July 2021, relative to the averaged densities measured during the first time interval from 1 September 2018 to 31 January 2019 for **a,** the Minamidake crater, **b,** the Showa crater, and **c,** the Reference region, respectively. The points refer to the mids of time intervals. Vertical ground deformations measured at the ten selected locations (Figure 1a) are shown by the red-coloured lines. The eruption frequency of Minamidake crater is shown by the black histogram.

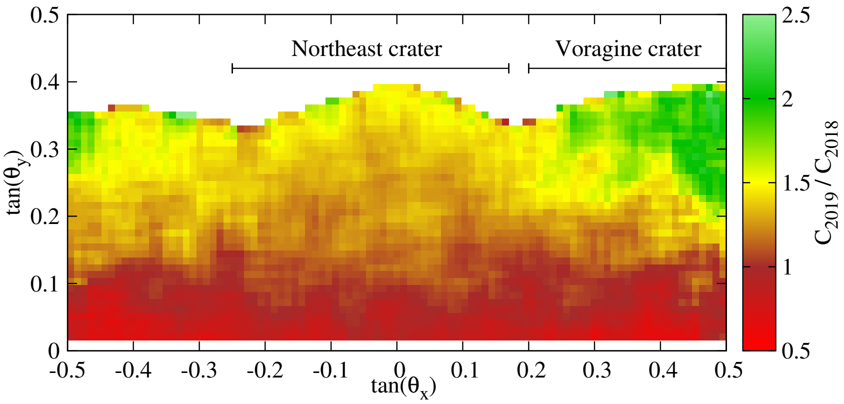

Figure 4. A muographic image of Mount Etna. The ratio of the forward to backward muon flux ratio measured for 2019 (C_{2019}) to the same quantity measured for 2018 (C_{2018}) is shown for each angular bin. The muographic observation was conducted at latitude 37.757 °N and longitude 14.988 °E, at a distance of 700 m in northwest from the Northeast Crater. Black arrows show the horizontal extensions of the Northeast crater and the Voragine crater, respectively. The current analysis was conducted based on the data provided by Lo Presti et al. (2022).